Numerical Simulation of the Zeeman Effect from Laser-induced Fluorescence of Neutral Xenon

IEPC-2007-254

Presented at the 30^{th} *International Electric Propulsion Conference, Florence, Italy*
September 17-20, 2007

Baïlo B. Ngom,
Timothy B. Smith,
Wensheng Huang,
and Alec D. Gallimore
University of Michigan, Ann Arbor, MI 48109

We present a numerical method for solving the components of magnetic field intensities relative to the axis of a tunable continuous-wave diode laser, which induces fluorescence from xenon particles downstream of a Hall thruster. The algorithm uses a non-linear least-squares error minimization techique based on the interior-reflective Newton approach for large scale optimization problems to resolve magnetic field components from the absorption spectrum of the particles undergoing $6S'\,[1/2] \rightarrow 6P'\,[3/2]$ **transition at 834.682 nm-vacuum. Aside from fine structure, the coupling between the species inherent hyperfine structure and Zeeman Effect induced by an external magnetic field characterize the absorption line spectrum. Our fitting model uses Bachers method of calculating Zeeman-hyperfine energy splitting and intensities of** σ **and** π**-transition lines, respectively, corresponding to perpendicular and parallel exciting light polarizations. Lorentz-Doppler broadening of the transition-line spectrum models to good accuracy measured spectra of neutral xenon in an opto-galvanic cell subject to various external magnetic field intensity settings. These latter measurements also validate our routine for minimizing the error between predicted and measured absorption line spectra for optimal magnetic field intensities. Voigt-profile modeling of line spectra makes it possible to estimate plasma kinetic temperature assuming elastic collisions. These efforts precede our ultimate goal of sketching the magnetic field distribution in a Hall thruster plume via application of the non-linear solver to neutral and ion absorption lineshapes resulting from diode laser-induced fluorescence spectral data. A spatial distribution of magnetic field intensity will help better understand failure mechanisms in Hall thrusters necessarily to improvements in the design of thrusters.**

I. introduction

Studies of electric thruster topologies have thus far relied on software-based modeling and physical probe-based measurements. Both these methods have limited field-mapping capabilities. In the former, the modeling is restricted to a vacuum environment of a "cold" thruster that only generates a magnetic field. Alone, such a configuration, does not make possible any prediction on the interaction betweeen magnetic field and plasma. When combined with physical probing, vacuum field simulations do, to a certain extent, allow such study. However, such measurements are intrusive due to the often non-negligible level of field contamination induced by current carrying physical probes[12] .[?] This makes probe-size reduction to sub-millimeter magnitudes the main recourse to reducing intrusiveness, but at the expense of higher sensitivity to failure. That is why, there has been growing interest in laser-induced fluorescence (LIF); the non-intrusive nature of this optical technique makes it an attractive for estimating magnetic field topology in electric thruster discharges through spectral analysis. When subject to the external effect of field-generating thruster-magnets, energy levels of plasma-discharge particles split; thereby, affecting LIF spectra. In this work, we apply an exact non-linear model to capture the Zeeman effect on the hyperfine structure of neutral xenon (Xe I) to model the effect of an external magnetic field on the species' absorption spectra as they undergo excitation by a laser-beam polarized perpendicularly with respect to the field direction. In anticipation of Hall-thruster LIF data exhibiting Zeeman splitting, we limit this preliminary work to the simpler case of an opto-galvanic cell immersed within the external magnetic field produced by Helmholtz coils. Successful spectral data fitting of the model prompted the development of a magnetic field intensity and kinetic temperature solver, which we validate in this work using optogalvanic spectra measurements at various field intensity levels spanning [30, 300] Gauss[14]—a practical intensity range reflecting field magnitudes in Hall-thrusters.

II. Theory of the non-linear Zeeman effect on hyperfine structure

Zeeman effect refers to a splitting of an atom's energy-levels that occurs when a magnetic field is externally applied to it. More fundamentally, it results from interactions of the magnetic field with momenta associated with orbital motions of a nucleus and electrons. In the classical world, an analogous phenomenon is the mechanical moment exerted on a current carrying circular wire along a direction normal to surface intersecting magnetic field lines. A theory dating back to the 1930s and developed by Sommerfeld, Heisenberg, Lande, and Pauli (cited in[4]) accurately models the zeeman effect on a spinning spherical charged body in orbital motion in a central force field and under an externally applied magnetic field using a complex matrix formulation. To describe the theory, Darwin uses the simpler formulation of wave-mechanics .[4,5] An application of the theory to natural elements is found in,[1] in which Bacher computes splittings of thallium and bismuth hyperfine lines in the 300-500 nm wavelength range and successfully validates it against observed spectra. Though useful, the theory has been, for the most part, ignored among the engineering community due to the complex nature of computations involved for elements with high momentum quantum numbers. As a recourse, a common trend has been to use approximative methods suited for low and high magnetic field intensities; These are respectively termed Pashen-Back and Anomalous Zeeman models.
Modern days' advances in computing capabilities, render modeling of the Zeeman effect on the hyperfine structure of hydrogenic element a trivial task; Still a good grasp and, hence, application of the exact theory to a specie like xenon, which consists of isotopes with and without hyperfine structure requires a brief introduction to the two approximative models of relevance to this work.

A. Approximative models in high and low-field limiting cases

Nuclear spin imposes a two-level categorization of approximative models more thoroughly described in.[7]

1. The linear Zeeman and Pashen-Back effects on the hyperfine structure

The Zeeman effect on the hyperfine applies to elements with non-zero nuclear spin subject to low external magnetic field intensities. In the vector representation, the model predicts a precession of the total angular momentum ($\vec{F}$ resulting from IJ-coupling) of the atomic system about the direction of the magnetic field lines ($\vec{B}$). Combined with the quantized nature of $\vec{F}$, this precession leads to in a magnetic moment μ_M proportional to a new quantum number M. The presence of quantized magnetic moments, in turn, gives rise to potential energies corresponding to new energy states resulting from F-levels' splittings. As expressed in

the following selection rules, F and M can only increase or decrease by 1 and span closed intervals:

$$|I - J| \leq F \leq I + J \text{ with } \Delta F = \pm 1 \tag{II.1}$$

$$-F \leq M \leq +F \text{ with } \Delta M = \pm 1 \tag{II.2}$$

The splitting of lines due to a field intensity B is given by:

$$\Delta E = \mu_M B = (g_F \mu_B M)B, \tag{II.3}$$

where g_F, the Lande-factor, is proportional to electronic and nucleic Lande-factors g_J and g_I, respectively. The other approximation results from the Pashen-Back effect on the hyperfine structure that applies to high external field intensities exerted on non-zero nuclear spin species. In this case, the potential also causes splitting of F-levels but arises from a lifting of IJ-coupling, which leads to independent precession of electronic and nucleic momenta about the field. As the field intensity increases, the angle between the direction of the field and the resulting quantized magnetic moment vectors μ_{M_J} and μ_{M_I} (respectively associated with a single valence electron' orbital motion and nucleus' spin) increases. The magnitudes of the quantized vectors are proportional to quantum numbers M_J and M_I; which, as in the low-field approximation, obey specific selection rules (refer to equations (II.12a) and (II.12b)).

$$-J \leq M_J \leq J \text{ with } \Delta M_J = \pm 1 \tag{II.4}$$

$$-I \leq M_I \leq I \text{ with } \Delta M_I = \pm 1 \tag{II.5}$$

2. The Anomalous Zeeman model

According to the Anomalous Zeeman theory, application of an external magnetic field of intensity B to xenon species without nuclear spin results in splitting J energy-levels into new M_J-levels. The energy displacements of these levels (eq. II.6) about a parent J-level are proportional to B and a magnetic moment μ_{M_J}; which in turn, is proportional to the quantum number M_J, whose admissible values are found from the selection rules in equation (II.12a). According to the vector model, J-level splitting results from various possible projections of the total angular momentum of the electron along the direction of the magnetic field as the momentum vector precesses about the latter while orbiting the nucleus. For such species, energy splittings solely depend on the quantum number $M_J$and the magnetic field intensity B, as indicated the following equation:

$$\Delta E = g_J M_J H \tag{II.6}$$

As shown below, the following simple algebraic formulas yield line intensities for $J \rightarrow J + 1$ transitions:

$$4(J^2 - {M_J}^2) \text{ for } M \rightarrow M \tag{II.7a}$$

$$(J - M_J + 1)(J - M_J + 2) \quad M \rightarrow M - 1 \tag{II.7b}$$

$$(J + M_J + 1)(J + M_J + 2) \quad M \rightarrow M + 1 \tag{II.7c}$$

All quantum numbers in the above equations are associated to initial states [a].
The Anomalous Zeeman theory is considered exact when applied to hydrogenic elements with no nuclear spin. But, at high magnetic field intensities, it consistutes a linear approximation for modeling spectra of elements with non-zero nuclear spin. Such a situation is fulfilled when the outer-electron's magnetic moment is much larger than that of the nucleus.

B. The non-linear Zeeman effect on hyperfine structure on hydrogen-like atoms

Because ranges of validity of high and low-field approximations vary from one element to the next, the non-linear Zeeman-hyperfine theory is the safest recourse to modeling spectra of spherically symmetric hydrogen-like atoms subject to an external magnetic field; the model captures an arbitrarily broad range of intermediate field strengths. An in-depth treatment of the theory is reported in.[1]

[a] in the remainder of this paper, we will use the terms initial and final to respectively denote J_1 and J_2 in a $J_1 \rightarrow J_2$ transition type

The time-independent Schrödinger wave equation (SE) (II.8) is a non-linear partial differential equation that governs the spatial evolution of a physical system's wave-function—an abstract concept that stores all physical information needed to fully describe a system.

$$\left(\frac{p^2}{2m} + V_E + V_{IJ} + V_{JB} + V_{IB}\right)\Psi = E\Psi, \tag{II.8}$$

where $\Psi = \Psi(\lambda, \chi, \mu, r, \theta, \varphi)$ is the wave-function of the atomic system separable into wave-functions $\Psi_N = \Psi_N(\lambda, \chi, \mu)$ and $\Psi_E = \Psi_E(r, \theta, \varphi)$; respectively associated to the nucleus and the outer-electron, whose motions are expressed in separate eulerian polar coordinate systems specific to each. The left-hand side of the equation consists of the Hamiltonian or energy operator acting upon the wave-function and accounting for (from left to right) the free particles' kinetic energy (first term) and coulombic interaction (V_E), which are both inherent to the atomic system system and lead to its fine structure; while the remaining three terms account for the separate and combined interactions of the nucleus spin motion and the electron's orbital motion with the magnetic field. Assuming that the latter two effects are separable, the overall wave-function assumes:

$$\Psi(\lambda, \chi, \mu, r, \theta, \varphi) = \Psi_E(r, \theta, \varphi)\,\Psi_N(\lambda, \chi, \mu). \tag{II.9}$$

Solution to SE. Inserting (II.9) into (II.8) and solving for the resulting equation leads to the following exact solution:

$$\Psi^{M_J, M_I}(\lambda, \chi, \mu, r, \theta, \varphi) = \sum_{M_J, M_I} X_{M_J, M_I}\Psi_E^{M_J}(r, \theta, \varphi)\,\Psi_N^{M_I}(\lambda, \chi, \mu), \tag{II.10}$$

where the wave-functions for the nucleus are:

$$\Psi_E^{M_J}(r, \theta, \varphi) = f(r)P_J^{M_J}(\cos\theta)e^{iM_J\varphi} \tag{II.11a}$$

$$\Psi_N^{M_I}(\lambda, \chi, \mu) = P_I^{M_I}(\cos\chi)e^{i(M_I\lambda + \tau\mu)}, \tag{II.11b}$$

and the quantum numbers $M_J$and $M_I$obey the following selection rules:

$$-J \le M_J \le J \tag{II.12a}$$

$$-I \le M_I \le I \tag{II.12b}$$

To find the system's characteristic equation, one inserts (II.11a) and (II.11b) into (II.10), then into the SE (II.8); before integrating over the space enclosing outer-electron and the nucleus subspaces. The characteristic equation (II.13) relates each possible energy state to a set of probability amplitudes of the wave-functions:

$$\begin{aligned} &-\left[\frac{a}{2}(J - M_J + 1)(I + M_I + 1)\right]X_{M_J-1, M_I+1} \\ &-\left[\frac{a}{2}(J + M_J + 1)(I - M_I + 1)\right]X_{M_J+1, M_I-1} \\ &+\left[E_{M_J, M_I} - a\,M_J\,M_I - (M_J g_J + M_I g_I)\;o\,H\right]X_{M_J, M_I} = 0, \end{aligned} \tag{II.13}$$

In the characteristic equation, H denotes the magnetic field strength in units of Tesla so that the energy eigenvalues turn out in units of cm^{-1}—unit-base upon which the characteristic equation's scaling has performed. The term $o = \frac{e}{4\pi mc^2}$ denotes the Larmor precession frequency in cgs units. Though computations were carried in the latter units, the results expressed in this paper are in SI units for practical purposes; hence, we will be refering to the magnetic field intensity B (in Gauss) in place of the strength H and express all energies in the more familiar GHz unit.

As it will become more evident in a practical example (see Section 2), equation (II.13) is a discrete eigen-value problem. Considering n possible energy states, a convenient expression of the latter equation is possible in matrix form:

$$[\mathrm{X}]_{n\times n}[\mathrm{E}]_{n\times n} = [\mathrm{C}]_{n\times n}[\mathrm{X}]_{n\times n}, \text{where} \tag{II.14}$$

[E] is a diagonal matrix of all containing the energy levels shifted about a parent J-level

[X] is a symmetric matrix consisting of vectors whose components are mode-shape amplitudes $X^{J,F}_{M_J, M_I}$ associated with each state

[C] is a matrix whose components are the coefficients in front of each X in equation (II.13)

RULES ON OPTICAL TRANSITIONS dicate permissible optical transitions; that is, changes of energy state that occurs when light excites an atomic system at the proper wavelength. An atom may undergo a transition between two states of respective wave-functions $\Psi^{M_J M_I}$ and $\Psi^{M'_J M'_I}$, only if their sums obey specific rules that depend on the polarization of the exciting radiation with respect to the direction of the external magnetic field line at some point where light emission or absorption of the species is being monitored. Table B summarizes rules on sums $M = M_J + M_I$ and $M' = M'_J + M'_I$ for each transition type. For example, in the case of emission, the energy ΔE lost by an atom in the form of light as it switches from an upper level E_M to a lower level $E_{M'}$, is termed transition-line energy.

Polarization	Transition	
	Label	ΔM
Parallel	π	0
Normal	σ^+	1
	σ^-	-1

Table 1. Transition rules on $\Delta M = M' - M$; with $M = M_J + M_I$ and $M' = M'_J + M'_I$ for σ and π-type transitions

THE STRENGTH OF RADIATIVE SPECTRAL LINES is proportional to the probability that the state of the system undergoes the change $\Psi^{M_J M_I} \rightarrow \Psi^{M'_J M'_I}$, as expressed below:

$$I = \frac{\left| \int \Psi^* \, \Psi' R d\tau \right|^2}{\int |\Psi'|^2 \, d\tau \;\; \int |\Psi'|^2 \, d\tau}, \tag{II.15}$$

where R, the polarization of the electric moment, depends on the type of transiton as expressed below:

$$R = \begin{cases} 2r\cos\theta & \text{for } \pi\text{-transitions } (M \rightarrow M) \\ r(e \pm i\phi \sin\theta) & \text{for } \sigma\text{-transitions } (M \rightarrow M \pm 1) \end{cases} \tag{II.16}$$

Successively replacing R by the appropriate expressions in (II.16) into (II.15) yields the following intensity formulae only valid to the specific subset of $J \rightarrow J-1$ interactions[b]:

- for π-transitions:

$$I = 4 \frac{\left[\sum_M X^{J,F}_{M_J,M_I} X^{J-1,F'}_{M'_J,M_I} (I+M_I)!(I-M_I)!(J+M_J)!(J-M_J)! \right]^2}{N^{J,F}_M N^{J-1,F}_M} \tag{II.17}$$

- for $\sigma^{\pm}$-transitions:

$$I = \frac{\left[\sum_M X^{J,F}_{M_J,M_I} X^{J-1,F'}_{M'_J \pm 1,M_I} (I+M_I)!(I-M_I)!(J+M_J)!(J-M_J)! \right]^2}{N^{J,F}_M N^{J-1,F}_{M\pm 1}} \tag{II.18}$$

The Shape-factors' normalization constants appearing in the denominators of (II.17) and (II.18) assume the general form for an arbitrary state of sum M.

$$N^{J,F}_M = \sum_M (X^{J,F}_{M_J,M_I})^2 (I+M_I)!(I-M_I)!(J+M_J)!(J-M_J)! \tag{II.19}$$

The homogeneous nature of equation (II.13) makes the mode-shape factors X arbitrary to within an arbitrary factor. However, the normalization condition makes it possible to uniquely define shape-factors $Y^{J,F}_{M_J,M_I}$:

[b] still the intensity equations are applicable to $J \rightarrow J+1$ transition by switching initial and final states

$$Y^{J,F}_{M_J,M_I} = \frac{X^{J,F}_{M_J,M_I}}{\sqrt{N^{J,F}_{M}}}; \tag{II.20}$$

replacing $X^{J,F}_{M_J,M_I}$ by $Y^{J,F}_{M_J,M_I}$ into (II.19) forces $N^{J,F}_{M}$ to assume a value of unity. For the sake of minimizing the number of variables, we will continue denoting normalized shape-factors by X. The summations over M in equations (II.17), (II.18), and (II.19) are to be interpretated as sums over all states satisfying $M_J + M_I = M$.

As a word of caution, it is worthwhile mentioning that the only quantum numbers needed to fully specify a quantum state in the non-linear Zeeman -hyperfine model are the set (J,F,M_J,M_I); which, we will whenceforth denote $\left|JFM_JM_J\right\rangle$—following Paul Dirac's convenient state-space vector notation:[10] $\left|JFM_JM_I\right\rangle$. Though, useful in determining quantum numbers $M_J$and M_I, M only takes part in describing states in the linear model of the Zeeman effect on hyperfine structure. This will become evident in a forcoming illustration, where we will show that many states can share a similar value for M. Were M to be a quantum number, the Pauli Exclusion principle would violated. Another way to interpreted such peculiarity is to consider states with common M values as arising from a lifting of degeneracies associated with M-levels in the Pashen-Back picture as the field strength rise high enough to cause distinguishable precession of $\vec{J}$and $\vec{I}$about $\vec{B}$.

Returning to Dirac's notation, an arbitrary transition J → J' can be interpreted as a projection of $\left|JFM_JM_I\right\rangle$ onto $\left|J'F'M'_JM'_I\right\rangle$: $\left\langle JFM_JM_I\middle|J'F'M'_JM'_I\right\rangle$. This permits a convenient representation of an arbitrary line transition's energy (E) and strength (I) into matrix format as shown below:

	$\left\langle J'F'M'_JM'_I\right\vert$
$\left\langle JFM_JM_I\right\vert$	(E,I)

Table 2. Using a single cell to illustrate a state-to-state interaction matrix

III. Simulation of Xe I absorption spectrum based on the Zeeman-HFS model

A. Determination of transition energies and line intensities

The first step in modeling the absorption spectrum of Xe I for the $6S'\,[1/2] \rightarrow 6P'\,[3/2]$ transition consists of computing energies associated with all possibles quantum states. But, the fact that xenon has nine stable isotopes (Ref.[6] requires different approaches. We apply the full non-linear Zeeman on hyperfine structure model to species with nuclear spin and the Anomalous Zeeman model to those without nuclear spin.

1. Case of isotopes without nuclear spin

Figure (1) shows the possible energy levels arising from upper and lower parent J-levels and all allowed transitions. Energies were computed using equations (II.6), respectively. The diagram applies to all isotopes without nuclear spin. Based on this fact alone, all such isotopes should have the same transition energy. However, each undergoes a particular shift arising from two separate effects (Ref[9] and[14]):

> a mass effect due to differences in the number of neutrons, which affects the binding energy in the center-of-mass coordinate of the atom
>
> a field effect due to differences in the shape and size of the charge distribution of protons within the nucleus

In this paper, all shifts are reported relative to ^{132}Xe; which, in terms of natural occurrence, constitutes the most abundant xenon isotope.

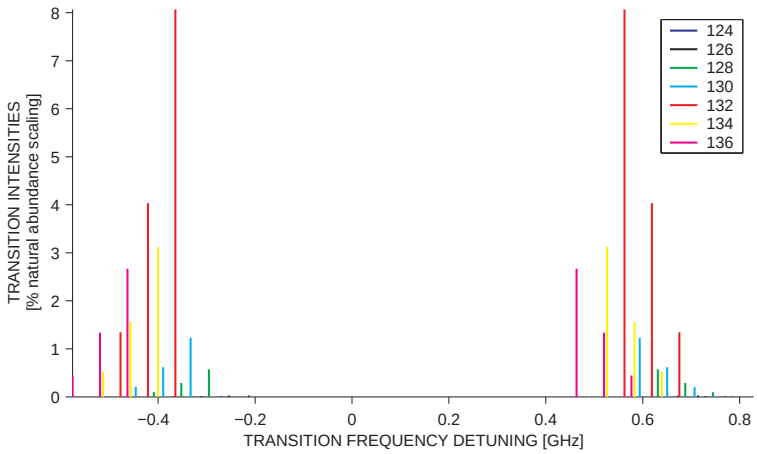

Figure 1. Line spectrum of xenon isotopes with no nuclear-spin

Application of the intensity formulae in eq. (II.7) (section 2), directly yields normalized line intensities plotted in fig.1 as a function of detuning frequency. Each set of lines has been scaled according to the percent natural abundance of each isotope (see Table 1).

Mass number	124	126	128	130	132	134	136
Abundance [%]	0.1	0.09	1.91	4.1	26.9	10.4	8.9
Shift [MHz]	279.8(30)	238.6(30)	197.45(30)	151.7(21.3)	110.1(11.3)	74.0(11.1)	0

Table 3. Isotopic shifts[17] and natural abundance[6] of stable xenon species with no nuclear spin

2. Case of isotopes with nuclear spin

COMPUTATION OF ENERGY STATES As a practical illustration of the Zeeman-HFS approach, we will use the simpler case of the initial state within the $[6S'\,[1/2] \rightarrow 6P'\,[3/2]]$ transition of ^{129}Xe for which $J = 1$ and $I = 1/2$.
Because each quantum state is defined by $\left|JFM_JM_I\right\rangle$, we start by determining all allowed values for F, M_J, and M_I using (II.1), (II.12a), and (II.12b), respectively. The scheme is shown in table (2).

F		M_J			M_J	
$\frac{1}{2}$	$\frac{5}{2}$	-1	0	1	$-\frac{1}{2}$	$\frac{1}{2}$

Table 4. Possible F, M_J, and $M_I$values for $6S'\,[1/2]$ state

To each F-number is associated a corresponding set of sums M given by (II.2); which, in turn, provides means for coupling M_J and M_I to form a particular state $\left|JFM_JM_I\right\rangle$ (see equation (II.2)). The simple process (summarized below) reveals six possible states for $6S'\,[1/2]$ ($\left|i\right\rangle, i = 1 \ldots 6$ - labels are respectively associated to states starting from left to right in the diagram below).

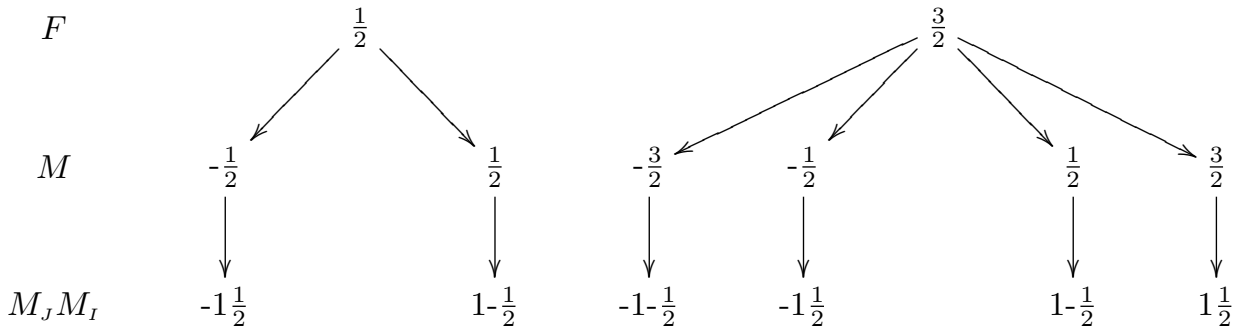

Comparing $\left|1\right\rangle = \left|1\tfrac{1}{2}\text{-}1\tfrac{1}{2}\right\rangle$ and $\left|4\right\rangle = \left|1\tfrac{3}{2}\text{-}1\tfrac{1}{2}\right\rangle$, we make the important observation that it is indeed possible for multiple states to have equal M-sums. As an upcoming discussion will clarify; it will be useful to denote a state or group of states with quantum numbers' sum M and corresponding sub-equation(s), eigen-values, and vectors with an M-prefix (for example M-state).

Based on optimal[c] hyperfine and magnetic constants constants hyperfine and magnetic constants with reported uncertainty bounds, we successively evaluate the characteristic equation (II.13) for each possible state $\left|i\right\rangle$ to arrive at the following eigenvalue problem (recall eq. II.14) for $H = 312$ Gauss. for the sake of clarity, only the i^{th} set of eigen-value and vector are shown.

$$\left\{ E^{\left|i\right\rangle}[\,\mathrm{I}\,] \begin{bmatrix} -2.32 & 0 & 0 & 0 & 0 & 0 \\ 0 & -1.85e-4 & -5.81 & 0 & 0 & 0 \\ 0 & -2.90 & 3.48 & 0 & 0 & 0 \\ 0 & 0 & 0 & 2.33 & -2.90 & 0 \\ 0 & 0 & 0 & -5.81 & 1.85e-4 & 0 \\ 0 & 0 & 0 & 0 & 0 & -3.45 \end{bmatrix} \right\} \begin{bmatrix} X_{1,1/2}^{1,3/2} \\ X_{0,1/2}^{1,3/2} \\ X_{1,-1/2}^{1,1/2} \\ X_{-1,1/2}^{1,3/2} \\ X_{0,-1/2}^{1,1/2} \\ X_{\text{-}1,\text{-}1/2}^{1,3/2} \end{bmatrix}^{\left|i\right\rangle} = [0] \qquad \text{(III.1)}$$

The energy eigenvalues $E^{\left|i\right\rangle}$[d] correspond to the roots of determinant of the term between curly brackets in equation (III.1). We used Matlab's built-in functions SCHUR and EIG to properly match eigen-values and vectors with states. SCHUR returns a triangular-matrix decomposition of the coefficient matrix as follows: $[C] = [U][T][U^T]$, where [U] is a unitary matrix, [T] is an upper-triangular matrix whose diagonal contains the sought eigenvalues arranged according to the order of sub-equations associated to states of specific sums M within (II.13)—denoted M-equations, henceforth. We then used EIG to solve for both eigen-values (again) and vectors; however, this function returns eigen-values and vectors inconsistently with M-equations' arrangement. We used a 'position-mapping' between eigenvalue sets generated by each function to properly reorder eigen-vectors.

Next, we performed (M_J,M_I)-state-to-energy mapping. Within M-states, energy levels needed to be mapped in increasing order of M_J. Table 2 displays the results from applying the process.

From computed eigen-vectors, we deduced normalized mode-shape amplitudes associated with initial states of ^{129}Xe as listed in table 2. Extension of the approach to the more complex case of 6P′ [3/2], for which $J = 2$ and $I = 1/2$ resulted in table 2.

The determination of energy levels of ^{131}Xe follows a similar approach to the one outlined above but is computationally more involved in that this isotope has a larger nuclear spin (recall Table 2)—hence, resulting in larger coefficient matrices. Table 2 and 2 respectively lists 12 initial states and 20 final states along with corresponding energy levels.

THE SPECTRUM OF LINE INTENSITIES followed from the knowledge of states energies and normalized mode-shapes (recall section B). Application of transition rules (Table B) and intensity formulae (II.18) directly yielded σ-transition line strengths and energies listed in the entries of the state-interaction matrix in diagram 2.

[c] Averaged optimal constants from table 2

[d] The numbering of energy levels is arbitrary.

Mass Number	129	131	Ref.
I	$\frac{1}{2}$	$\frac{3}{2}$	6
μ_N $[(\frac{m_p}{m_e})^{-1}]$	-0.7768(0.0001)	0.700(0.05)	?
A [GHz]	-5801.1(12.8)	1713.7(6)	17
	-2892.4(6.9)	858.9(3.1)	8
g_J	1.321	1.321	13
	1.190(0.001)	1.190(0.001)	2

Table 5. Physical parameters associated with stable isotopes ^{129}Xe and ^{131}Xe having hyperfine structure. Upper and lower sub-rows are respectively associated with initial and final states. From μ_N and I, we deduced Lande-$g_I$factor using: $g_I = (\frac{m_p}{m_e})^{-1}\frac{\mu_N}{I}$, where the proton-to-electron mass ratio $\frac{m_p}{m_e} = 1836$. The numbers between parentheses are uncertainty widths (e.g. 1.190(0.001) is equivalent to 1.190 $\pm$ 0.001) that, in some cases, incorporate widths by other authors cited within listed sources.

State	Energy	Mode-shape amplitudes					
	[GHz]	$X^{1,3/2}_{1,1/2}$	$X^{1,3/2}_{0,1/2}$	$X^{1,1/2}_{1,-1/2}$	$X^{1,3/2}_{-1,1/2}$	$X^{1,1/2}_{0,-1/2}$	$X^{1,3/2}_{-1,-1/2}$
$\left\|1\frac{3}{2}1\frac{1}{2}\right\rangle$	-2.33	0.707	-	-	-	-	-
$\left\|1\frac{3}{2}0\frac{1}{2}\right\rangle$	-2.72	-	-0.834	0.552	-	-	-
$\left\|1\frac{1}{2}1\text{-}\frac{1}{2}\right\rangle$	6.20	-	-0.390	-0.590	-	-	-
$\left\|1\frac{3}{2}\text{-}1\frac{1}{2}\right\rangle$	-3.10	-	-	-	0.426	0.564	-
$\left\|1\frac{1}{2}0\text{-}\frac{1}{2}\right\rangle$	5.43	-	-	-	0.798	-0.603	-
$\left\|1\frac{3}{2}\text{-}1\text{-}\frac{1}{2}\right\rangle$	-3.50	-	-	-	-	-	0.577

Table 6. ^{129}Xe upper state's ($6S'[1/2]$) energy levels along with corresponding mode-shape amplitudes

State	$\left\|2\frac{5}{2}2\frac{1}{2}\right\rangle$	$\left\|2\frac{5}{2}1\frac{1}{2}\right\rangle$	$\left\|2\frac{3}{2}2\text{-}\frac{1}{2}\right\rangle$	$\left\|2\frac{5}{2}0\frac{1}{2}\right\rangle$	$\left\|2\frac{3}{2}1\text{-}\frac{1}{2}\right\rangle$	$\left\|2\frac{5}{2}\text{-}1\frac{1}{2}\right\rangle$	$\left\|2\frac{3}{2}0\text{-}\frac{1}{2}\right\rangle$	$\left\|2\frac{5}{2}\text{-}2\frac{1}{2}\right\rangle$	$\left\|2\frac{3}{2}\text{-}1\text{-}\frac{1}{2}\right\rangle$	$\left\|2\frac{5}{2}\text{-}2\text{-}\frac{1}{2}\right\rangle$
Label	$\left\|1\right\rangle$	$\left\|2\right\rangle$	$\left\|3\right\rangle$	$\left\|4\right\rangle$	$\left\|5\right\rangle$	$\left\|6\right\rangle$	$\left\|7\right\rangle$	$\left\|8\right\rangle$	$\left\|9\right\rangle$	$\left\|10\right\rangle$
Energy (GHz)	-1.85	-2.28	-5.28	-2.69	4.66	-3.11	4.04	-3.52	3.41	-3.93

Table 7. ^{129}Xe final state's ($6P'[3/2]$) energy levels

State	$\left\|1\frac{5}{2}1\frac{3}{2}\right\rangle$	$\left\|1\frac{5}{2}0\frac{3}{2}\right\rangle$	$\left\|1\frac{3}{2}1\frac{1}{2}\right\rangle$	$\left\|1\frac{5}{2}\text{-}1\frac{3}{2}\right\rangle$	$\left\|1\frac{3}{2}0\frac{1}{2}\right\rangle$	$\left\|1\frac{1}{2}1\text{-}\frac{1}{2}\right\rangle$	$\left\|1\frac{5}{2}\text{-}1\frac{1}{2}\right\rangle$	$\left\|1\frac{3}{2}0\text{-}\frac{1}{2}\right\rangle$	$\left\|1\frac{1}{2}1\text{-}\frac{3}{2}\right\rangle$	$\left\|1\frac{5}{2}\text{-}1\text{-}\frac{1}{2}\right\rangle$	$\left\|1\frac{3}{2}0\text{-}\frac{3}{2}\right\rangle$	$\left\|1\frac{5}{2}\text{-}1\text{-}\frac{3}{2}\right\rangle$
Label	$\left\|1\right\rangle$	$\left\|2\right\rangle$	$\left\|3\right\rangle$	$\left\|4\right\rangle$	$\left\|5\right\rangle$	$\left\|6\right\rangle$	$\left\|7\right\rangle$	$\left\|8\right\rangle$	$\left\|9\right\rangle$	$\left\|10\right\rangle$	$\left\|11\right\rangle$	$\left\|12\right\rangle$
Energy (GHz)	3.15	-1.50	2.94	-4.55	-1.60	2.72	-4.18	-1.75	2.49	-1.97	2.25	2.00

Table 8. ^{131}Xe initial state's ($6S'[1/2]$) energy levels

State	$\left\|2^{\frac{7}{2}}2^{\frac{3}{2}}\right\rangle$	$\left\|2^{\frac{7}{2}}1^{\frac{3}{2}}\right\rangle$	$\left\|2^{\frac{5}{2}}2^{\frac{1}{2}}\right\rangle$	$\left\|2^{\frac{5}{2}}0^{\frac{3}{2}}\right\rangle$	$\left\|2^{\frac{5}{2}}1^{\frac{1}{2}}\right\rangle$	$\left\|2^{\frac{3}{2}}2^{-\frac{1}{2}}\right\rangle$	$\left\|2^{\frac{7}{2}}{}_{-1}{}^{\frac{3}{2}}\right\rangle$	$\left\|2^{\frac{5}{2}}0^{\frac{1}{2}}\right\rangle$	$\left\|2^{\frac{3}{2}}1^{-\frac{1}{2}}\right\rangle$	$\left\|2^{\frac{1}{2}}2^{-\frac{3}{2}}\right\rangle$	$\left\|2^{\frac{7}{2}}{}_{-2}{}^{\frac{3}{2}}\right\rangle$	$\left\|2^{\frac{5}{2}}{}_{-1}{}^{\frac{1}{2}}\right\rangle$	$\left\|2^{\frac{3}{2}}0^{-\frac{1}{2}}\right\rangle$	$\left\|2^{\frac{1}{2}}1^{-\frac{3}{2}}\right\rangle$	$\left\|2^{\frac{7}{2}}{}_{-2}{}^{\frac{1}{2}}\right\rangle$	$\left\|2^{\frac{5}{2}}{}_{-1}{}^{-\frac{1}{2}}\right\rangle$	$\left\|2^{\frac{3}{2}}0^{-\frac{3}{2}}\right\rangle$	$\left\|2^{\frac{7}{2}}{}_{-2}{}^{-\frac{1}{2}}\right\rangle$	$\left\|2^{\frac{5}{2}}{}_{-1}{}^{-\frac{3}{2}}\right\rangle$	$\left\|2^{\frac{7}{2}}{}_{-2}{}^{-\frac{3}{2}}\right\rangle$
Label	$\left\|1\right\rangle$	$\left\|2\right\rangle$	$\left\|3\right\rangle$	$\left\|4\right\rangle$	$\left\|5\right\rangle$	$\left\|6\right\rangle$	$\left\|7\right\rangle$	$\left\|8\right\rangle$	$\left\|9\right\rangle$	$\left\|10\right\rangle$	$\left\|11\right\rangle$	$\left\|12\right\rangle$	$\left\|13\right\rangle$	$\left\|14\right\rangle$	$\left\|15\right\rangle$	$\left\|16\right\rangle$	$\left\|17\right\rangle$	$\left\|18\right\rangle$	$\left\|19\right\rangle$	$\left\|20\right\rangle$
Energy (GHz)	3.60	0.364	3.33	-2.02	0.0970	3.05	-3.57	-2.23	-0.201	2.76	-4.53	-2.72	-0.532	2.46	-3.25	-0.888	2.16	-1.27	1.85	1.53

Table 9. ^{131}Xe final state's ($6P'\,[3/2]$) energy levels

	$\left\|1\right\rangle$	$\left\|2\right\rangle$	$\left\|3\right\rangle$	$\left\|4\right\rangle$	$\left\|5\right\rangle$	$\left\|6\right\rangle$	$\left\|7\right\rangle$	$\left\|8\right\rangle$	$\left\|9\right\rangle$	$\left\|10\right\rangle$
$\langle 1\vert$	(-0.37,7.6)	(6.2,0.82)	-	-	(0.20,3.3)	(7.8,1.1)	-	-	-	-
$\langle 2\vert$	(-8.7,0.0025)	(-2.2,9.6)	-	-	(-8.2,0.00043)	(-0.55,3.6)	-	-	-	-
$\langle 3\vert$	-	-	(0.40,6.9)	(8.5,0.73)	-	-	(-0.21,4.0)	(6.9,0.95)	-	-
$\langle 4\vert$	-	-	(-8.8,0.00085)	(-0.74,10)	-	-	(-9.4,0.0011)	(-2.3,3.1)	-	-
$\langle 5\vert$	-	-	-	-	(-0.076,2)	(7.5,2)	-	-	(0.56,12)	-
$\langle 6\vert$	-	-	-	-	-	-	(-0.020,2)	(7.1,2)	-	(-0.55,12)

Table 10. Energies(GHz) and normalized intensities of σ-transition lines in ^{129}Xe: $6S'\,[1/2]\rightarrow 6P'\,[3/2]$

Applying the above approach to ^{131}Xe, reveals 74 σ-transitions. The overlaid spectrum in figure 2 illustrates the shifting due to each isotope. Furthermore, the normalized line intensities have been scaled to account for relative natural abundances. Table 2 provides shifts and percent abundances associated of each isotope. Figure 2 showing σ^- transitions completes the spectrum of lines.

Masse number	129	131
Shift [MHz]	213.4(4.7)	189.7(6.1)
Abundance [%]	26.4	21.2

Table 11. Isotope energy shifts[17] and natural abundances[6] of stable xenon species with non-zero nuclear spin

Broadening of lines To simulate the warm spectrum $W(\nu)$ or absorption spectrum of xenon atoms in the plasma environment, we apply a Voigt profile[7] to the spectrum of transition lines $Y(\nu)$; such a profile accounts for two predominant physical phenomena: the Heisenberg Uncertainty Principle (HUP) and the thermal motion of particles—assumed to be at equilibrium. As expressed in (III.2), the profile results from the convolution of a cold spectrum $C(\nu)$ with a maxwellian distribution.[15]

$$W(\nu) = C(\nu) \otimes D(\nu), \quad \text{where} \tag{III.2}$$

$$D(\nu) = exp\left[\frac{M}{2kT}(\lambda_o \nu)^2\right] \tag{III.3}$$

The HUP enters in the picture through C, which results from Lorentz broadening. As expressed in (III.4), the effect is simulated by convolving Y with a Lorentzian lineshape $L(\nu)$ defined in (III.5).

$$C(\nu) = L(\nu) \otimes Y(\nu), \quad \text{where} \tag{III.4}$$

$$L(\nu) = \sum_i^n \frac{1}{\pi} \frac{\Delta\nu}{(\nu - \nu_i)^2 + (\Delta\nu)^2}, \quad \text{where} \tag{III.5}$$

the summation in (III.5) accounts for all lines (numbered $i = 1, 2, \ldots, n$) and $\Delta\nu = \frac{A_{ij}}{2\pi}$ is the width of individual lines at half-maximum. Figure 2 respectively illustrate how Lorentizian and Doppler broadening lead to the sought Voigt profile. We set A_{ij} to $8.8110^6 sec^{-1}$ based on a reported value of $6.3610^6 sec^{-1}$ (uncertainty $\pm 40\%$)[e] (see C).[11]

[e]optimal physical parameters are all within bounds of uncertainties reported by their authors and were found based on a best fit of the non-linear least-squares approach discussed in C

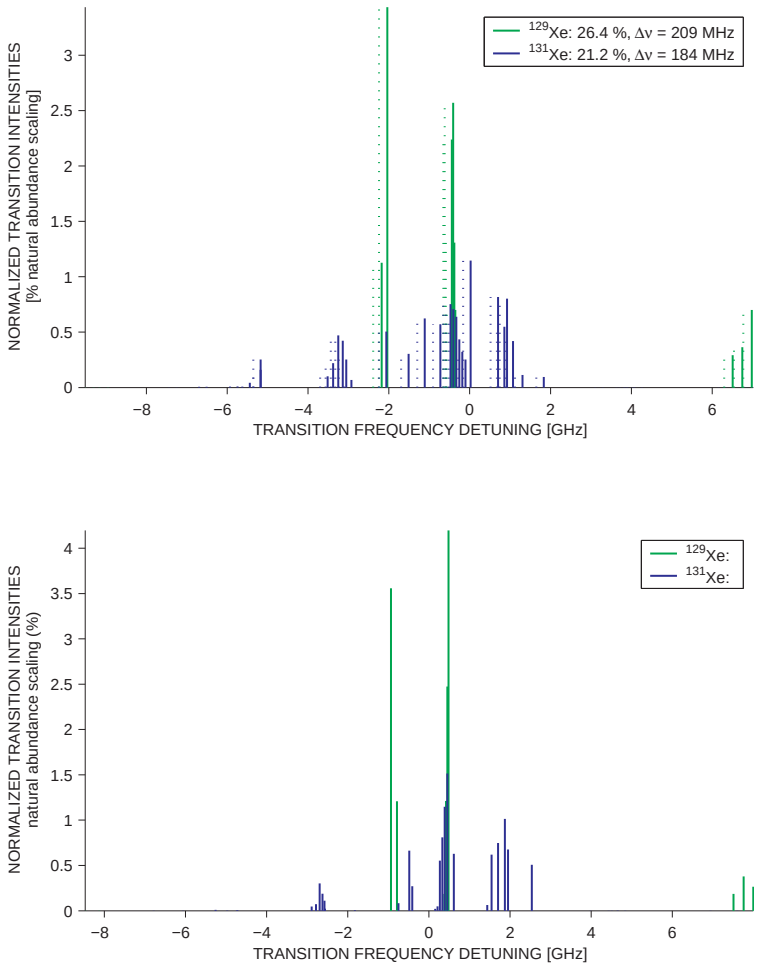

Figure 2. σ^- and σ^+ transition line strengths of ^{129}Xe and^{131}Xe. Unshifted lines appear dashed.

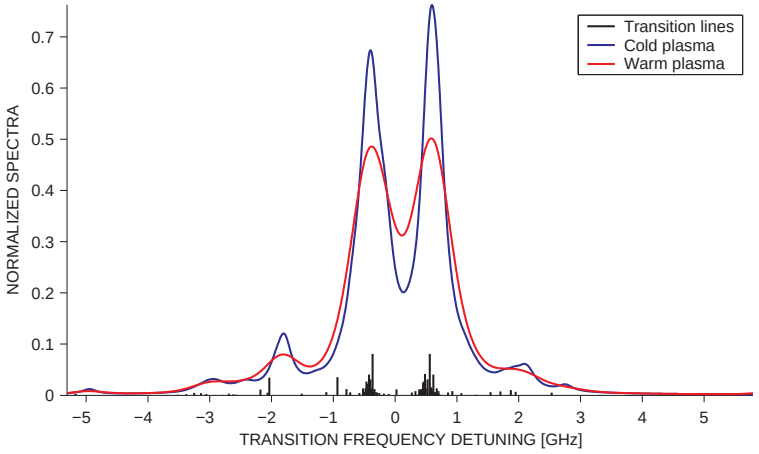

Figure 3. Illustration of Voigt profile generation from the spectrum of transition lines. The cold and warm spectra shown are based on Lorentz and Doppler broadenings of transition lines. H = 300 Gauss in this plot

IV. Validation of the computational model

A. Experimental setup

We used spectral data from a galvatron to validate the non-linear Zeeman-HFS model. A detailed description of the experiment—performed at the University of Michigan's (UM) Plasma dynamics and Electric Propulsion Laboratory (PEPL)—can be found in.[16] The simple device consists of a glass tube filled with xenon and argon (non-reacting filler) bottle. It encloses two electrodes for plasma breakdown. The galvatron is calibrated such that when the plasma is exited by a light source tuned to a particular transition's wavelength, its voltage output varies proportionally with the radiative intensity of the gas absorption. The exciting light source consists of a tunable single-mode diode-laser centered at 834.682 nm (air-wavelength of the $6S'[1/2] \rightarrow 6P'[3/2]$ transition). Scans spanned 10 GHz mode-hop-free frequency detuning ranges. A 2 GHz free-spectral-range (FSR) Fabry-Perot interferometer accurate to 6.7 MHz insured high-resolution detuning. A pair of Helmholtz coils was placed on either side of the galvatron so that their symmetry axis is perpendicular to the galvatron's axis. The error on field strength measurements was estimated at 2%. This arrangement permitted the generation of a variable external field of maximal strength along the path of the laser, which stimulated the optogalvanic effect as it propagated through the cylindrical electrodes within the spread of the plasma. To excite π or σ-transitions, the laser was polarized in front of the galvatron's input aperture. A lock-in amplifier operating with a time-constant of 300 ms read output voltages and relayed them to a PC; the latter controlled the voltage of the laser's piezo-electric tuning element over 10 Volt-span ramp.

B. Continuity of transition energies and and smooth distribution of absorption spectra

As mentioned in B, the non-linear Zeeman-hyperfine model is, in theory, applicable to an arbitrarily wide range of field strengths—machine tolerance being the only constraint, the range extends from 0.01 to 50,000 Gauss. For the purpose of investigating field strengths in electric thrusters, this limitation poses no problem since typical field strengths fall well within that range (0 to 200 gauss).[12] Figures B and B, respectively, illustrate continuous variations of transition energies from 0.01 to 1000 Gauss for ^{129}Xe and ^{131}Xe. Because the energies resulting from the characteristic equation (equation (II.13)) denote shift with respect to some hypothetical level (^{1}), we had to shift transition energies about the center of gravity of the lines; that is, transition energies were weighted with respected to corresponding intensities.
Energy level continuity led to smooth variations of cold and warm spectra with magnetic field intensity. Figure B illustrates this through a surface plot of Xe I cold spectrum about 834.682 nm.

C. Solving for the magnetic field strength and plasma temperature using a non-linear least-squares method

Description of the non-linear least-squares solver We applied Matlab's built-in function LSQNONLIN to our optimization problem. It finds optimal design paramaters $\boldsymbol{p^*} = \boldsymbol{p^*}(p_1^*, p_2^*, \ldots p_k^* \ldots p_n^*)$ that minimize a smooth non-linear function of the type $\epsilon(\boldsymbol{p}) = \frac{1}{2}\sum_i (T_i(\boldsymbol{p}) - E_i)^2$ while parameters are constrained within closed-bound intervals. Starting with a guessed set of parameters $\boldsymbol{p^o} = \boldsymbol{p^o}(p_1^o, p_2^o, \ldots p_k^o \ldots p_n^o)$, the method allows the progression of $\epsilon(\boldsymbol{p})$ towards the minimum $\epsilon(\boldsymbol{p^*})$ of the error function by iterative steps of optimal lengths along steepest descent search directions corresponding to $\nabla\epsilon$ at Iterative points towards the point of convergence. Convergence of the solver to an optimal point or solution is achieved when the change in the norm of the residual[f] falls below a tolerance level. This novel non-linear method,[3] which suited for large scale problems of many variables is more efficient than traditional linear optimization techniques in its interior-reflective Newton line-search technique that allows a quadratic decay in the residual norm and insures global minimization of the error function. The efficiency stems primarily from the fact that $\boldsymbol{p}$ progresses towards $\boldsymbol{p*}$ along a feasible region—the bounded path, along which $\boldsymbol{p}$ progresses [g]. An affine transformation of the vector space defined by $\boldsymbol{p_k}(k = 1, 2, \ldots, n)$ and successive reflections of steepest descent directions with respect to prior ones about the normal of the feasible region at each point (in a piece-wise fashion) generates a search path that remains well centered between the boudaries—key to fast and robust

[f] the residual, which is not to be confused with the error between fit and experiment, is related to the gradient of the error function at some point of the iteration path leading to the point of convergence

[g] The interior-reflective Newton method deviates from lesser efficient traditional methods like the Simplex method which causes a marching of $\boldsymbol{pm}$ along the boundaries[3]

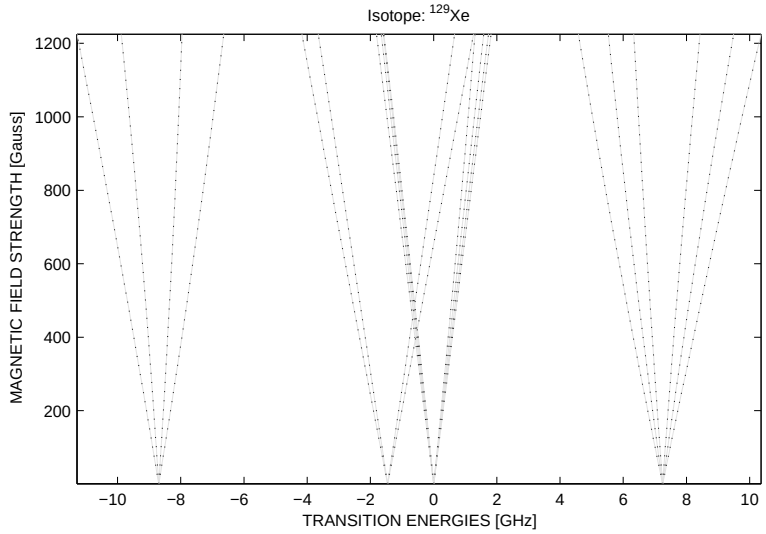

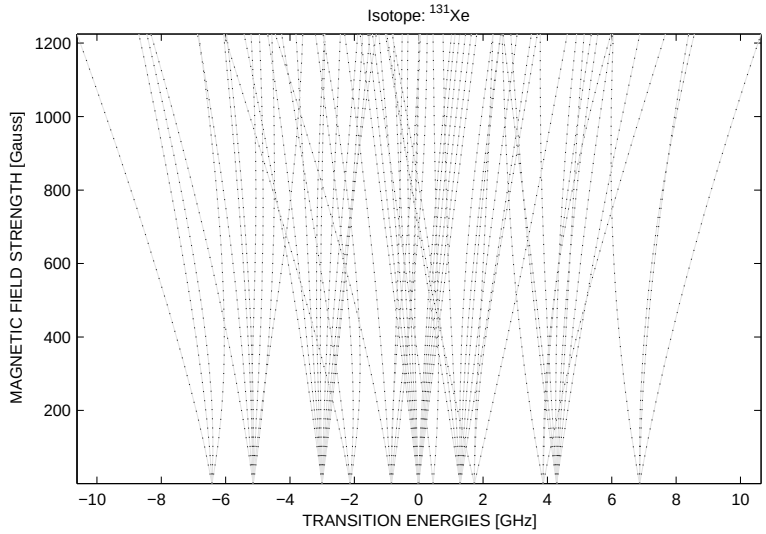

Figure 4. Variation of transition energies of ^{129}Xe and^{131}Xe with magnetic field strength

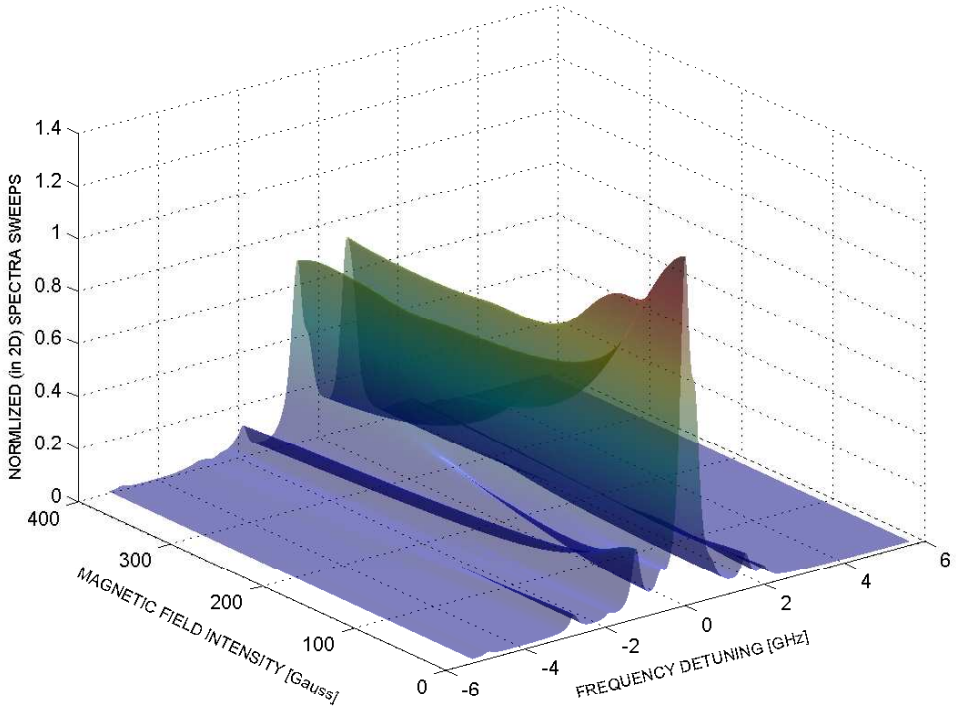

Figure 5. Smooth surface distribution of cold spectra with respect to magnetic field intensity

convergence.

We determined optimal physical parameters and target solutions as a preamble to solving for the external magnetic field intensity and plasma kinetic temperature from remote initial guesses. Because mere use of p_o would not necessarily yield the best predictions on galvatron's plasma temperature and the external field strength, we solved for the optimal variables within their respective uncertainty bounds. We also determined target external magnetic field intensities and plasma kinetic temperatures. By 'target', we mean our best estimates of experimental settings within reported uncertainty bounds.
We treated all unknown parameters as components of a vector $\boldsymbol{p}$ bounded within

$$p \in [p_{min}, p_o[\bigcup]p_o, p_{max}],$$

where p_o denotes a vector of error interval centers reported in tables 2, 1, and 2. We set the tolerance of the solver to 10^{-7} to match the resolution of the galvatron's voltage measurements and frequency detuning [h]. and that of the frequency detuning [i].
We used LSQNONLIN to solve for $\boldsymbol{p^*}$ listed in table C at field strength intensities spanning 30 to 300 gauss. The table also lists averages $\overline{p^*}$ (right-end of table) and relative deviations of error functions (bottom-end of table) $\Delta^*_\epsilon = \frac{\epsilon^* - \epsilon_o}{\epsilon_o}$ and $\Delta_{\overline{\epsilon^*}} = \frac{\overline{\epsilon^*} - \epsilon_o}{\epsilon_o}$. At all field strength settings, a reduction of the error function is evident. From table C, we also make the important observation that $\Delta_{\overline{\epsilon^*}} \approx \Delta_{\epsilon^*}$; A priori, this prompts us to consistently use $\overline{p^*}$ as optimal input physical parameters to the temperature and field-strength solver for fitting any σ-spectral distribution excited by an arbitrary external field of strength falling within the investigated range $[30, 300]$.
In addition to the physical parameters mentionned above, optimal field intensities were simultaneously computed within some 100% error interval, which we set wide in the hope to account for experimental errors (see section A) and any shifts from interactions between plasma-induced and the external magnetic field.

[h]The precision level of spectral intensity measurements was 10^{-7} V and was limited by the lock-in amplifier's sensivity or maximum bits sent to the PC

[i]The resolution on frequency detuning of 6.710^{-3} GHz (recall A) translates to $2.010^{-7} cm^{-1}$

Table C reports the resulting effective (or 'target') field intensities corresponding to each particular set of parameters at the various B_{exp} settings [j] included for comparison. We treated the computed optimal values, not measured external field intensities, as target values for the B and T solver—described and validated in section C. We note that target field intensities are better matches to measured center values as the latter increase. The 120-Gauss setting separates a group of poorer from better matches.

[j] recall that B_{exp} corresponds to measured maximal strengths along the center axis of the current-carrying coils

		Magnetic field strengths (Gauss)										
Center		33.19	65.6	99.01	131.9	164.8	197.8	230.8	263.7	296.7	329.7	**329.7**
Optimal		16.59	32.87	49.51	112.4	142.6	168.7	210.9	236.3	272.3	311.3	**311.3**
States	Isotopes	Optimal variables										**averages**
		Galvatron temperatures (K)										
		450	462.7	512.2	467.7	450.1	450.8	471.8	452.3	450	504.4	**467.2**
		Isotope shifts (MHz) - relative to 136										
	124	250.2	250.2	250.2	250.3	250.2	250.2	250.2	250.2	250.2	250.2	**250.2**
	126	209.1	209.1	209.1	209.1	209.1	209.1	209.1	209.1	209.1	209.1	**209.1**
	128	167.9	167.9	167.9	167.9	167.9	167.9	167.9	167.9	167.9	167.9	**167.9**
	129	208.7	208.7	208.7	208.7	208.7	208.7	208.7	208.7	208.7	208.7	**208.7**
	130	130.4	130.4	130.4	130.4	130.4	130.4	130.4	130.4	130.4	130.4	**130.4**
	131	183.6	183.6	183.6	183.6	183.6	183.6	183.6	183.6	183.6	183.6	**183.6**
	132	98.9	98.9	98.9	98.91	98.9	98.9	98.9	98.9	98.9	98.9	**98.9**
	134	62.9	62.9	62.9	62.9	62.9	62.9	62.9	62.9	62.9	62.9	**62.9**
		Hyperfine constants (MHz)										
$6S'[1/2]$	129	-5811	-5811	-5786	-5811	-5786	-5786	-5804	-5786	-5811	-5811	**-5801**
	131	-2888	-2898	-2899	-2899	-2899	-2899	-2899	-2899	-2888	-2896	**-2897**
$6P'[3/2]$	129	1718	1718	1718	1718	1718	1718	1718	1718	1718	1718	**1718**
	131	855.8	855.8	855.8	855.8	855.8	855.8	855.8	855.8	855.8	855.8	**855.8**
		Electron Lande-g factors: g_J										
$6S'[1/2]$		1.321	1.321	1.321	1.321	1.321	1.321	1.321	1.321	1.321	1.321	**1.321**
$6P'[3/2]$		1.189	1.189	1.189	1.189	1.189	1.19	1.189	1.189	1.189	1.191	**1.189**
		Nuclear moments: μ_N										
	129	-0.7769	-0.7767	-0.7767	-0.7767	-0.7767	-0.7767	-0.7767	-0.7767	-0.7769	-0.7769	**-0.7768**
	131	0.6498	0.6498	0.6498	0.7498	0.7498	0.7498	0.7498	0.7498	0.7498	0.7498	**0.7198**
		Einstein emission coefficient										
		0.7997	0.8903	0.8904	0.8904	0.8904	0.89	0.8904	0.8904	0.8897	0.8904	**0.8812**
		Percent relative error from center										
		-107.6	-96.02	-115	-158.9	-218.3	-266.4	-240.1	-336.4	-353	-229.1	**-193.2**

Table 12. Determination of Optimal Physical Parameters for Input in Temperature and Field Strength Solver

To predict magnetic field intensity and kinetic plasma temperature along the axis of the galvatron, we used a separate LSQNONLIN solver from the previously described one. In this case, $\epsilon = \epsilon(B, T)$ was to be minimized. The solver used averaged optimal isotope shifts, hyperfine constants, and Lande-factors expressed in table C) to compute the error function at each iteration. Figure 6(a) illustrates good experimental spectrum fitting for a field intensity of 270 Gauss. Above the plot is listed starting guesses H_o and T_o; solutions H^* and T^*; and deviations Δ_H and Δ_T of the solutions from target values. The latter two parameters are means to assessing the quality of the convergence; the smaller the deviations, the better the matching of optimal solutions to target values. Figure 6(b) displays the initial guess with respect and the computed solution on a surface plot of $\epsilon(B, T)$ and further validates the smoothness of the latter function and convergence of the solver to a global minimum. The table accompanying figure 6(b) describes the convergence process in greater detail; note the non-linear steep decay of the size of the steps that the interior-reflective Newton line-search makes possible (C).
Good fits of various other settings spanning [30, 300] Gauss are illustrated in Figure 7. These reveal convergences to within 10 % of target temperatures and field intensities even with starting guesses deviating by a as much as 300 % from expected targets. Analysis of the convergence reveal the following key points:

1. We noted poorer convergence—but still on the fair order of 10 %—of the solver at field intensities above 120 Gauss. This is due to the fact that energy levels are in the order of 0.01 GHz below this value. This is in the order of $10^{-7} cm^{-1}$—the tolerance setting of the solver—hence reducing the quality of the convergence. As a remedy, we enlarged the variable space by including physical parameters listed in table C but keeping the uncertainty bounds unchanged and only relaxing field intensity and temperature bounds and corresponding initial guesses. As expected, this approach improved convergence because the interior-reflective Newton algorithm is best suited for large scale problems involving many unknowns to optimize.

2. The plasma kinetic temperature remained below 5 % at all settings. We expect this from the fact that the partial derivative of the error function respect to this variable is unaffected by the separation of energy levels; hence, tolerance settings do not affect its convergence.

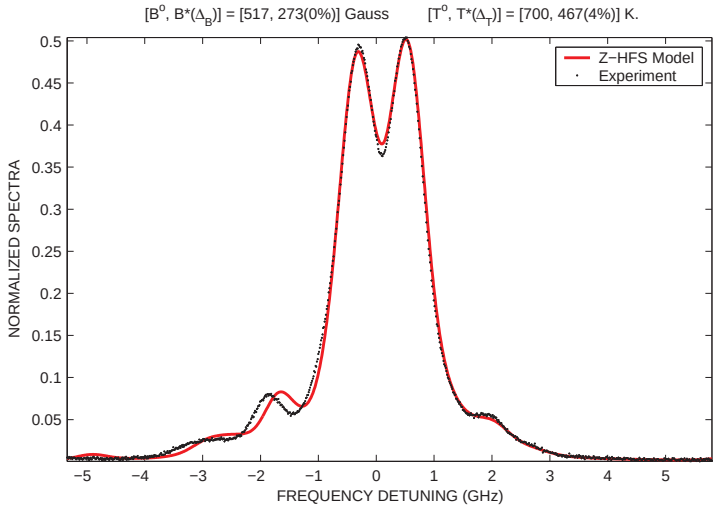

(a) Variation of fitting-error with B and T

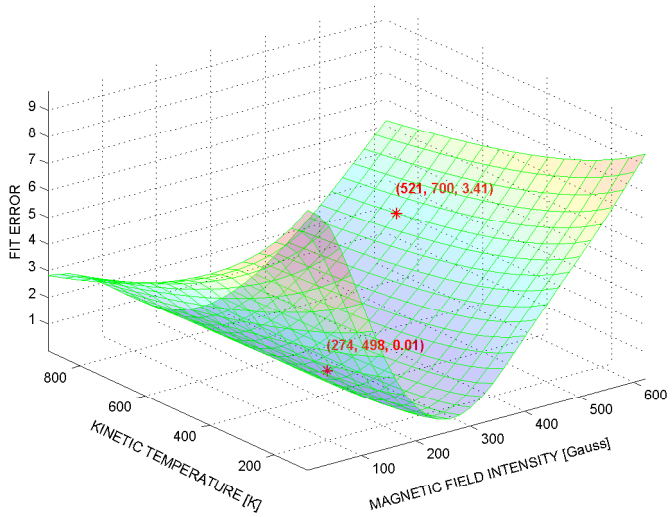

(b) Spectral fitting for optimal B and T

Iteration	$\epsilon(B,T)$	Norm of step
1	0.175723	1
2	0.053548	6.86105
3	0.0479	2.9966
4	0.0476004	0.82513
5	0.047596	0.104012

Figure 6. Computation of the external magnetic field intensity and plasma kinetic temperature in an opto-galvanic cell based non-linear least-squares fitting of the Xe I absorption σ-spectrum at 834.682 nm (in air) for a field setting of 270 Gauss

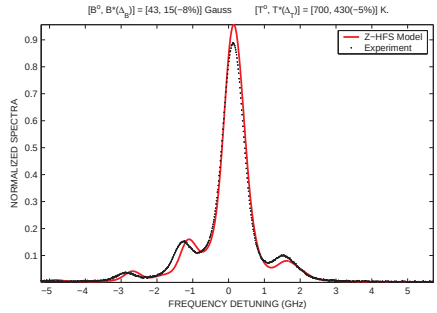

(a) 30 Gauss

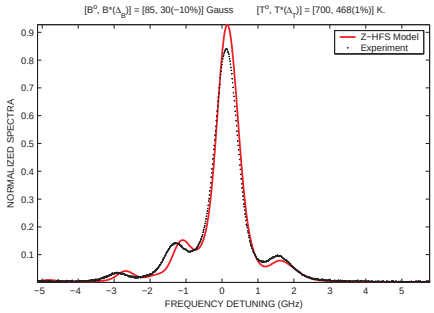

(b) 60 Gauss

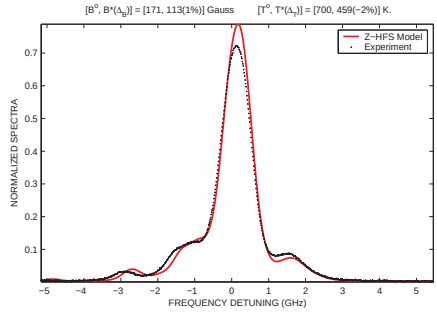

(c) 120 Gauss

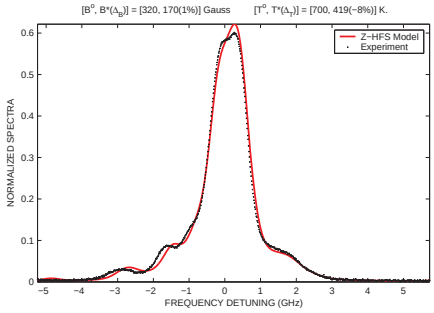

(d) 180 Gauss

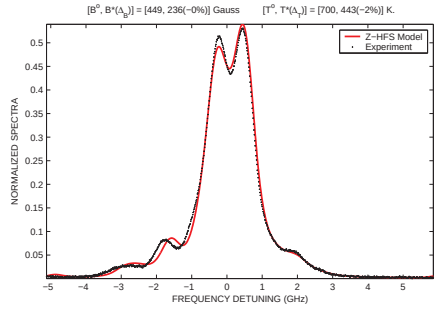

(e) 240 Gauss

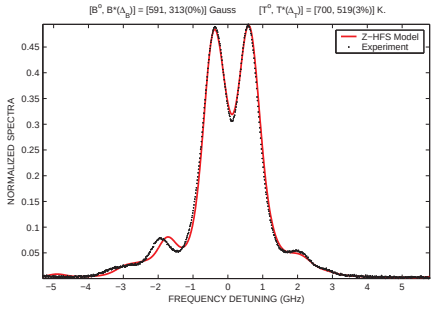

(f) 300 Gauss

Figure 7. Least-squares fitting of neutral xenon absorption spectra at 834.682 nm in an opto-galvanic cell at various external magnetic field intensity settings. The fitting is based on optimal magnetic field intensity and plasma kinetic temperature outputted by Matlab's LSQNONLIN solver.

Sensitivity of solver to signal-to-noise ratio Though the above analysis dealt with opto-galvanic spectra, we stress that the main goal of the solver is to resolve magnetic field intensities and kinetic temperatures from laser-induced fluorescence spectra measured in electric thruster discharges. The latter spectra are typically much noisier with signal-to-noise (SNR) ratios on the order of 100.[14] Hence, to further validate of the B and T solver, we studied the effect of gaussian noise addition to experimental spectra on convergence. We found little impact of random artificial noise on the quality of convergence at $SNR > 200$. And in some cases it actually, improved convergence. At high field intensity settings B-convergence remained good as illustrated in the fit of figure 8(a) at 30 Gauss despite the effect of tolerance setting on its convergence. At lower settings, however, convergence was poorer. The quality of convergence is better assessed from figures 8(b) and 8(c) showing the evolution of the devations of optimal variables from their corresponding target values with SNR. Gaussian noise had little effect on the convergence at SNRs above 200. And in some extreme cases such as the 30 Gauss setting shown on 8(a) at an SNR of 20, gaussian noise actually seems to help convergence; the quadratic nature of the error-function which relates it to the gaussian distribution of the random noise may be at the origin of this anomaly.

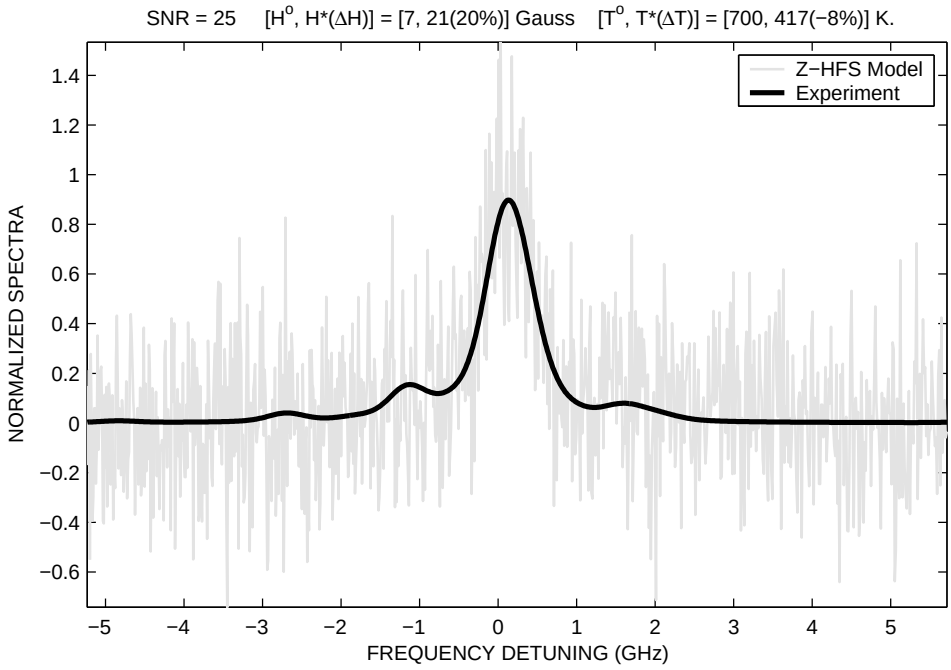

(a) Illustration of noisy spectrum fitting

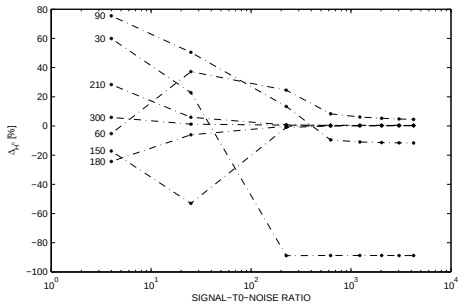

(b) Effect of SNR on B convergence

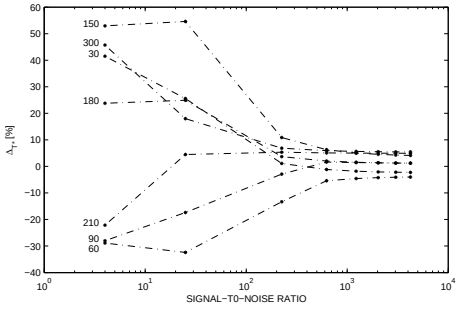

(c) Effect of SNR on T convergence

Figure 8. Effect of signal-to-noise ratio (SNR) on the optimization of external magnetic field intensity (B) and plasma kinetic temperature (T) of an opto-galvanic cell based on non-linear least-squares fitting of neutral xenon absorption spectra at 834.682 nm (in air)

V. conclusion

The non-linear Zeeman effect on the hyperfine structure is to-date the most accurate theory for modeling of hydrogen-like atomic spectra. We successfully used it to model neutral xenon absorption spectra in the plasma environment produced within an opto-galvanic cell to which an external magnetic field was applied. The reliability of the model prompted us to use it at a input function to a non-linear solver of magnetic intensity and kinetic plasma kinetic temperature based on best experimental spectra fitting. We noted good convergence of the solver in both variables even in the presence of Gaussian noise, provided the signal-to-noise ratio (SNR) remained above 200. At lower SNRs, errors on optimal values with respect to expected target solutions still remained below 80 %. Overall, we noted similar convergence of kinetic temperature at all field intensities investigated, but differing convergence behaviors for magnetic field intensities; for the latter variable, we noted poorer convergence at low field settings. The results found in this study make our non-linear solver a good computational tool for the study of the interaction between external magnetic field and xenon Hall thruster discharges as well as for thermal speed extraction from LIF spectra. More importantly, we project a trivial extension of the method to multiply-ionized xenon species, whose study may shed greater light on thruster-life limiting phenomena such as acceleration-grid and cathode erosions.

References

[1]R. F Bacher. *The Zeeman Effect of Hyperfine Structure*. PhD thesis, University of Michigan, Ann Arbor, MI, 1930.

[2]D. A. Bethe and R. R. Bacher. Nuclear physics a. stationary states of nuclei. *Review of Modern Physics*, 8, 1936.

[3]T. F. Coleman and Y. Li. On the convergence of interior-reflective newton methods for nonlinear minimization subject to bounds, 1994.

[4]C.G. Darwin. The zeeman effect and spherical harmonics. volume 115 of *Proceedings of the Royal Society of London. Series A*, pages 1–19, 1927.

[5]K. Darwin. Examples of the zeeman effect at intermediate strengths of magnetic field. volume 118 of *Proceedings of the Royal Society of London. Series A*, pages 264–285, 1928.

[6]R. B. Firestone. *Table of Isotopes*. Wiley, New York, 1999.

[7]H. Haken and H. C. Wolf. *The Physics of Atoms and Quanta*. Springer, Verlag Berlin Heidelberg, 7th edition, 1997.

[8]D. A. Jackson and M. C. Coulombe. Hyperfine structure in the arc spectrum of xenon. volume 327 of *Proceedings of the Royal Society of London. Series A, Mathematical and Physical Sciences*, pages 137–145, 1972.

[9]W. H. King. *Isotope Shifts in Atomic Spectra*. Plenum Press, New York, 1984.

[10]E. Merzbacher. *Quantum Mechanics*. Wiley, New York, 3rd edition, 1997.

[11]M. H. Miller, R. A. Roig, and R. D. Bengtson. Transition probabilities of xe i and xe ii. *Physical Review A*, 8(1), 1973.

[12]P. Y. Peterson, A. D. Gallimore, and J. M. Haas. Experimental investigation of a hall thruster internal magnetic field topography. 27th International Electric Propulsion Conference, Pasadena, CA, 2001.

[13]E. B. Saloman. Energy levels and observed spectral lines of xenon, xe i through xe liv. Technical report, National Institute of Standards and Technology, Gaithersburg, Maryland 20899-8422, 2004.

[14]T. B. Smith. *Deconvolution of Ion Velocity Distributions from Laser-Induced Fluorescence Spectra of Xenon Electrostatic Thruster Plumes*. PhD thesis, University of Michigan, Ann Arbor, MI, 2003.

[15]T. B. Smith, D. A. Herman, A. D. Gallimore, and R. P. Drake. Deconvolution of axial velocity distributions from hall thruster lif spectra. 27th International Electric Propulsion Conference, Pasadena, CA, 2001.

[16]T. B. Smith, W. Huang, B. B. Ngom, and A. D. Gallimore. Optogalvanic and absorption spectroscopy of the zeeman effect in xenon. 30th International Electric Propulsion Conference, Florence, Italy, 2007.

[17]M. Suzuki, K. Katoh, and N. Nishimiya. Saturated absorption spectroscopy of xe using a gaas semiconductor laser. *Spectrochimica Acta Part A*, 58:2519–2531, 2002.